

Reports on ICON



Subgrid scale Lightning Potential Index for ICON with parameterized convection

Guido Schröder, Tobias Göcke, Martin Köhler
August 2022

DOI: 10.5676/DWD_pub/nwv/icon_010

ISSN: 2628-4898



The CC license "BY-NC-ND" allows others only to download the publication and share it with others as long as they credit the publication, but they can't change it in any way or use it commercially.

Publisher

Deutscher Wetterdienst
Business Area "Research and Development"
Frankfurter Straße 135
63067 Offenbach
www.dwd.de

Editors

Sebastian Rast, MPI-M
sebastian.rast@mpimet.mpg.de
René Redler, MPI-M
rene.redler@mpimet.mpg.de
Daniel Reinert, DWD,
daniel.reinert@dwd.de
Daniel Rieger, DWD,
daniel.rieger@dwd.de
Florian Prill, DWD,
florian.prill@dwd.de

Subgrid scale Lightning Potential Index for ICON with parameterized convection

Guido Schröder, Tobias Göcke, Martin Köhler

Deutscher Wetterdienst

This document refers to release icon-2.6.4-nwp5.

Abstract

A subgrid scale lightning potential index (LPI) based on parameterized deep convection as well as a modified version of this index (MLPI) have been developed and implemented in ICON.

It is based on the LPI formula of [Lynn and Yair \(2010\)](#) for models with resolved convection. Following the idea of [Lopez \(2016\)](#), the quantities (e.g. vertical velocity) needed in the LPI formula are derived from the updraft of the Bechtold-Tiedtke parameterization scheme ([Bechtold et al., 2008, 2014](#)). In case of MLPI the formula is further improved by taking into account the vertical equivalent potential temperature gradient (i.e. the KO-index). LPI and MLPI are tested in ICON with 20 km resolution (ICON-20).

The MLPI is verified against LINET lightning data ([Betz et al., 2009](#)) over central Europe for the months 06/07 2020 and 03/2021-08/2021. The MLPI is also compared to the LPI and the lightning flash density (LFD, Lopez, 2016), all computed in ICON-20. A grid scale verification for the test period shows that the MLPI outperforms the LPI and LFD. However, when the location error is removed, LPI performs best.

Keywords: Lightning, Deep convection

Correspondence to: Guido Schröder (guido.schroeder@dwd.de)

1. Introduction

The occurrence of lightning is difficult to predict with numerical models. Forecasters rely mostly on ingredient based methods taking into account large scale indices for moisture, instability, dynamically forced lifting and shear. These indices are usually derived from numerical model simulations.

They have also been used to understand the impact of climate change on thunderstorm occurrence. E.g., [Taszarek et al. \(2021\)](#) analyzed ERA5 data to find trends in environments beneficial for the development of thunderstorms and lightning in Europe and the US.

However, it is desirable to develop methods to forecast lightning directly. For numerical models, purely statistical methods are available. [Stoltz et al. \(2017\)](#) for example used a region dependent multi-linear regression model with global reanalysis data as predictors and the total lightning density as predictand.

For convection permitting models [Lynn and Yair \(2010\)](#) derived a lightning potential index (LPI) based on physical assumptions. This index has already been implemented in ICON in the past and can be used when using convection permitting resolutions like in ICON-D2. Their formulation requires information on the updraft region like the distribution of hydrometeors and the vertical wind speed.

For models with non-convection-permitting resolution the forecast of lightning is more complex. [Charn and Parishani \(2021\)](#) applied a superparameterization to a coarse resolution model where each grid box contained a nested cloud resolving model (CRM) with 2 km grid size. They tested several proxies, e.g. proxies based on the variables of the cloud microphysics schemes as well as more simple proxies like the product of CAPE and precipitation. They found that using a two-moment cloud microphysics scheme all indices have a higher correlation with lightning than using a one-moment scheme. The best performance had the GFLUX proxy for lightning based on [McCaull et al. \(2009\)](#) which corresponds to the vertical graupel flux at -15 °C in the updraft of the cloud.

[Tippett and Koshak \(2018\)](#) also used the product of CAPE and precipitation as a proxy for lightning. Using the NCEP Global Ensemble Forecast System (GEFS) they showed with this proxy that there is statistically significant skill to forecast lightning even for week 2.

[Lopez \(2016\)](#) developed a parameterization for the lightning flash density (LFD) for large scale models with parameterized deep convection based on physical assumptions. The LFD uses quantities from the Bechtold-Tiedtke parameterization scheme ([Bechtold et al., 2008, 2014](#)).

For ICON running with parameterized deep convection so far no lightning parameterization exists. An ideal parameterization would be simple and should have no significant impact on the runtime of ICON. Therefore, two indices have been implemented: the LFD as well as a new subgrid scale version of the LPI. Additionally, a modified LPI (MLPI) is developed that also takes into account the KO-index (e.g. [Ulbrich, 2016](#)).

Section 2 describes the derivation of the MLPI as well as the formulation of the subgrid scale LPI. Section 3 assesses the quality of MLPI in comparison to LFD and LPI using lightning observations. Section 4 examines the diurnal and annual cycle as well as the spatial distribution of observed and modeled lightning. Section 5 provides four case studies – one for each season. This report ends with a summary and conclusions in Section 6.

2. Description of the subgrid scale (M)LPI

The subgrid scale modified lightning potential index MLPI is based on the lightning potential index (LPI, [Lynn and Yair, 2010](#)) adjusted for use with parameterized convection and the vertical

equivalent potential temperature gradient, i.e. the KO-index (e.g. Ulbrich, 2016).

2.1. Description of the subgrid scale LPI

The LPI is defined in Lynn and Yair (2010) as

$$LPI = 1/V \int_{z_T=0^\circ C}^{z_T=-20^\circ C} \int \int \epsilon w^2 dx dy dz .$$

The integral is computed horizontally over one grid cell and vertically over the charge separation zone, i.e. over the area where the temperature is between $0^\circ C$ and $-20^\circ C$. Here V is the integration volume and w the vertical wind speed in the updraft. ϵ is defined as

$$\epsilon = 2 \frac{(Q_i Q_l)^{0.5}}{Q_i + Q_l} .$$

Here Q_l is the liquid water mixing ratio while Q_i is what Lynn and Yair (2010) call the ice fractional mixing ratio:

$$Q_i = q_g \left[\frac{(q_s q_g)^{0.5}}{q_s + q_g} + \frac{(q_i q_g)^{0.5}}{q_i + q_g} \right]$$

q_s , q_i , q_g are the mixing ratios of snow, ice and graupel, respectively.

In its original formulation the LPI can only be computed for numerical models where deep convection is resolved on the grid scale (e.g. in ICON-D2). For coarser resolutions with parameterized convection the grid scale LPI would be meaningless since deep convection takes place subgrid scale within the parameterization scheme.

Therefore all quantities needed for the computation of a LPI are in this case taken from the updraft of the Bechtold-Tiedtke parameterization scheme (Bechtold et al., 2008, 2014). w can be derived from the vertical kinetic energy which is directly computed in the convection scheme (see Eq. (3.12) in Bechtold, 2017). The mixing ratios have to be approximated.

The liquid water and ice mixing ratios are computed by splitting the updraft cloud condensate Q_{up} of the parameterization scheme into liquid and ice as follows:

$$Q_l = \alpha Q_{\text{up}} \\ q_i = (1 - \alpha) Q_{\text{up}} ,$$

with

$$\alpha = \max \left\{ 0, \min \left[1, \left(\frac{T - 250.15 \text{ K}}{23 \text{ K}} \right) \right] \right\}^2$$

In the code Q_{up} and the function α are named `plu` and `foealfa`, respectively.

Snow and graupel mixing ratios are computed as in Lopez (2016):

$$q_g = \beta \frac{P_f}{\rho_e v_g} \\ q_s = (1 - \beta) \frac{P_f}{\rho_e v_s} ,$$

with

$$\begin{aligned}\beta &= 0.70 \text{ over land} \\ \beta &= 0.45 \text{ over sea} \\ v_s &= 0.5 \text{ ms}^{-1} \\ v_g &= 3.0 \text{ ms}^{-1}\end{aligned}$$

Here P_f is the frozen precipitation flux of the updraft and ρ_e the environmental air density. In the remainder of this report the subgrid scale LPI will simply be referred to as LPI.

2.2. Derivation of MLPI

The subgrid scale LPI shows a good correlation with the occurrence of lightning. To show this the LPI has been computed for a period of 03/2019 to 02/2020 for member 1 of ICON-EU-EPS (grid 28, R02B07), herein called ICON-20. The forecasts are started from the ICON analysis every 3 hours for a lead time of up to 3 hours to make sure that the forecasts remain close to reality. The data (hourly maxima of LPI) on the unstructured grid has been interpolated with the nearest neighbor approach to a rotated regular lon/lat grid of 0.2 degrees resolution. For this grid the pole has been rotated to (170°E, 40°N).

For the same grid hourly counts of lightning per grid box using LINET lightning data ([Betz et al., 2009](#)) were computed (lightning density in $\text{km}^{-2}\text{hr}^{-1}$). The LPI data points of the whole 1 year period were sorted and equally sized bins of 10,000 data points were generated. Only the bin containing all LPI=0 is larger. For each bin the associated average observed lightning density was computed and multiplied by 400 km^2 to deal with convenient numbers. This means the numbers correspond to $20 \times 20 \text{ km}^2$ grid cells. In the remainder of this report this is referred to as lightning rate r_{400} measured in hr^{-1} . Fig. 1 shows that LPI and lightning rate are correlated (green line). However, it also shows shown that the KO-Index (KOI) provides some additional value.

The KO-index is defined as the vertical gradient of the equivalent potential temperature θ_e (e.g. [Ulbrich, 2016](#))

$$\text{KOI} = \theta_{e,600\text{hPa}} - \theta_{e,900\text{hPa}},$$

where $\theta_{e,600\text{hPa}}$ is the mean of θ_e within 700 hPa and 500 hPa and $\theta_{e,900\text{hPa}}$ is the mean of θ_e within the ground and 800 hPa. If the ground pressure is below 800 hPa, $\theta_{e,900\text{hPa}}$ is set to θ_e at the ground.

Again the sorted LPI values are binned – this time after being split in two parts – one where $\text{KOI} > 0$ and one where $\text{KOI} < 0$. For LPI below 100 J/kg there is a clear signal that higher lightning rates can be achieved when $\text{KOI} < 0$ (red circles and black squares in Fig. 1).

To understand the behavior of KOI better two-dimensional bins have been created for KOI and LPI and the mean lightning rate r_{400} is computed. From this a modified LPI (MLPI) is constructed. The idea is to derive an MLPI that has a similar behavior as the LPI but is more capable of discriminating between high and low lightning rate situations. To achieve this a linear

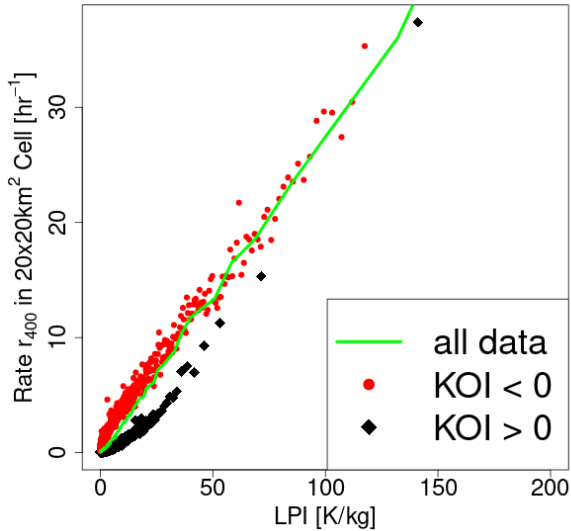


Figure 1: Lightning rate r_{400} per grid cell by LPI bin (green line). Stratified by KOI > 0 (black squares) and KOI < 0 (red circles). Based on LINET data.

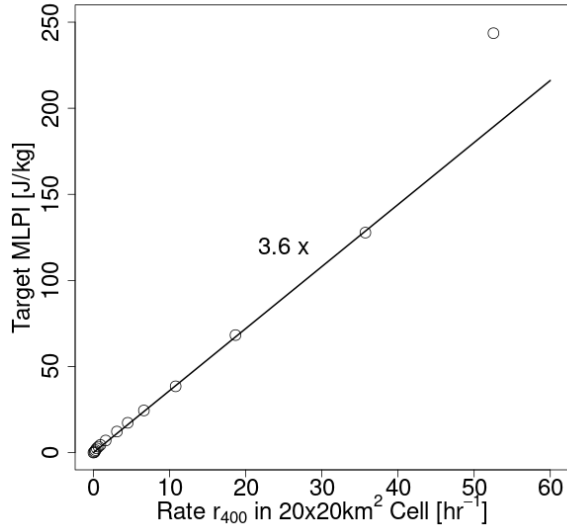


Figure 2: Conversion of the lightning rate r_{400} into a target MLPI. Circles are computed from LINET data.

conversion has been derived from lightning rates solely binned by LPI (Fig. 2, $\text{MLPI} = 3.6 * r_{400}$). This allows to convert the lightning rates into a target MLPI. Fig. 3 shows that KOI clearly has an impact on the MLPI that should be taken into account.

It is further assumed that the MLPI saturates for $\text{KOI} \rightarrow \pm\infty$. The range MLPI can have (as a function of LPI) is defined as

$$\begin{aligned}\text{MLPI}(\text{LPI}, \text{KOI} \rightarrow \infty) &= b(\text{LPI}) \\ \text{MLPI}(\text{LPI}, \text{KOI} \rightarrow -\infty) &= a(\text{LPI}) .\end{aligned}$$

The data also implies that for $\text{LPI} > 100 \text{ J/kg}$ the effect of KOI is not significant anymore (Fig. 1). Therefore we require

$$b(\text{LPI}) = a(\text{LPI}) = \text{LPI} \text{ for } \text{LPI} \geq \text{LPI}_c .$$

For $\text{LPI} < \text{LPI}_c$ we assume the following non-linear fit:

$$\begin{aligned}b(\text{LPI}) &= i \text{LPI}^j \\ a(\text{LPI}) &= g \text{LPI}^h\end{aligned}$$

The coefficients are obtained via optimization of the error of a and b , while the targets are taken from the binned data in Fig. 3. For a the average of the target MLPI for $\text{KOI} < -8 \text{ K}$ is used, for

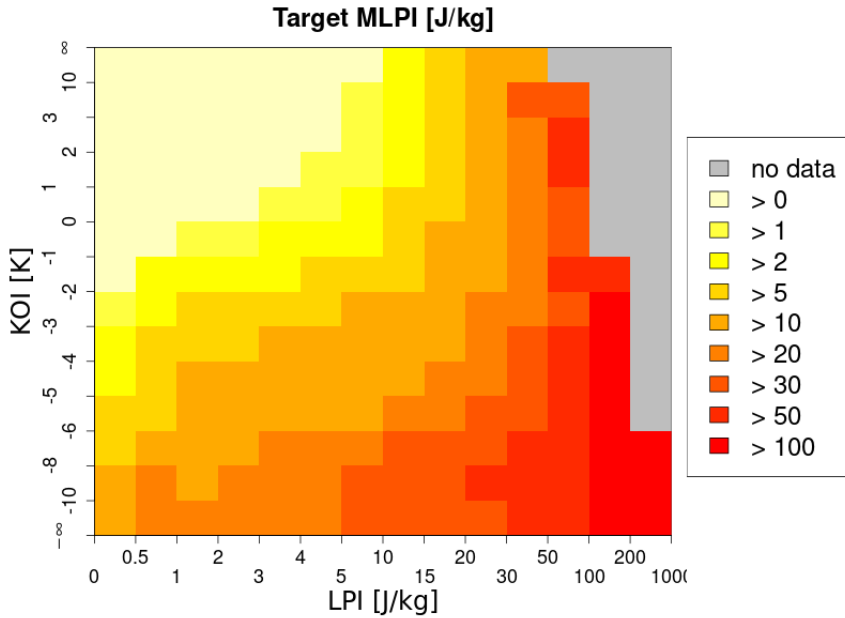


Figure 3: Target MLPI per grid cell by LPI and KOI bin.

b the average of the target MLPI for KOI > 0 K is used. The fit yields the following coefficients:

$$\begin{aligned} \text{LPI}_c &= 86.16 \text{ J/kg} \\ g &= 15.52 \\ h &= 0.385 \\ i &= 0.0424 \\ j &= 1.709 \end{aligned}$$

Fig. 4 shows the fit for *a* and *b*.

For constant LPI the MLPI varies between *a* and *b* depending on KOI. For the transition a sigmoid function is suitable. Here tanh is used and the binned data of Fig. 3. The following formula is optimized:

$$\text{MLPI}(\text{LPI}, \text{KOI}) = b(\text{LPI}) + 0.5 \{1 + \tanh[-e[\text{KOI} + d]]\} [a(\text{LPI}) - b(\text{LPI})] \quad (1)$$

with the coefficients optimized as

$$\begin{aligned} d &= 4.55 \\ e &= 0.296. \end{aligned}$$

Fig. 5 shows how often the different combinations of LPI and MLPI occur during the training period 03/2019-02/2020.

Fig. 6 shows the fitted MLPI in comparison to the binned target MLPI. The fit does not perform so well for small LPI < 2 J/kg and KOI < -4 K. For larger LPI the fit works well.

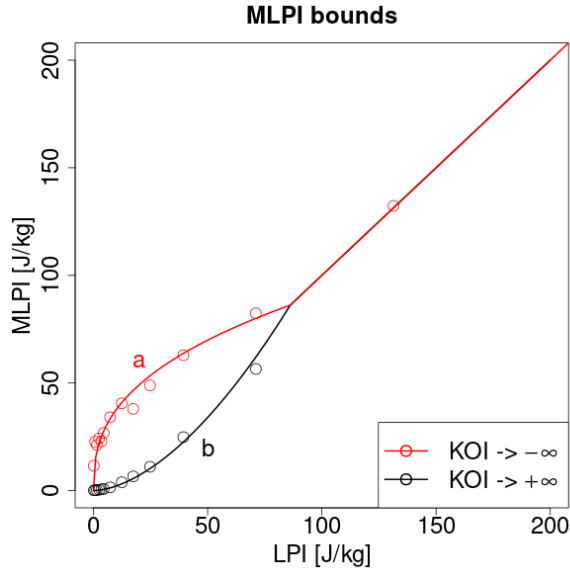


Figure 4: Bounds of MLPI by LPI for very large and very small KOI. Circles are derived from the target MLPI that was converted from the binned lightning rates (Fig. 3).

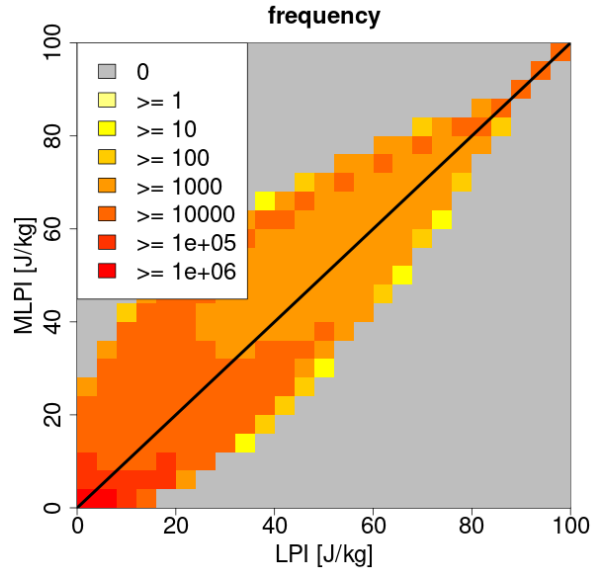


Figure 5: LPI versus MLPI - occurrence of pairs of values.

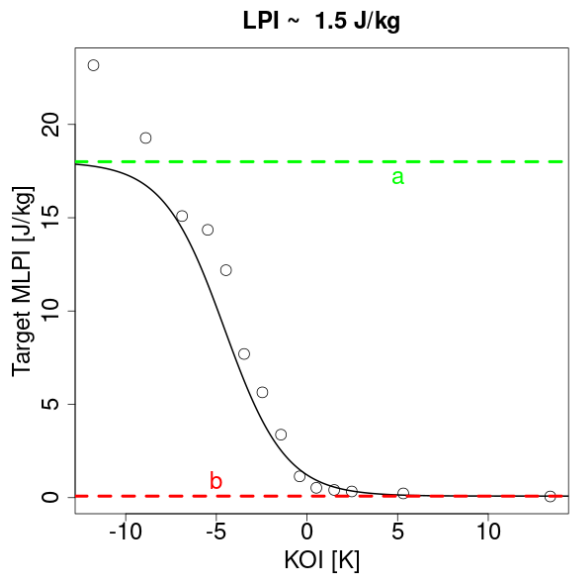
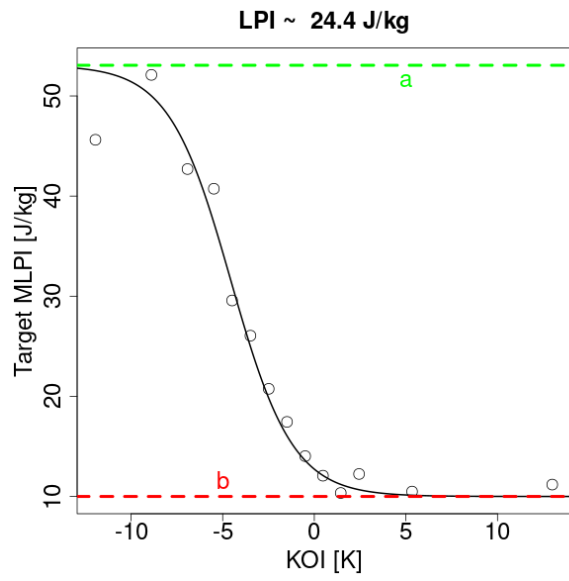


Figure 6: Example for the effect of KOI on MLPI. When LPI is fixed, MLPI decreases with decreasing KOI. The circles are based observations from LINET converted to virtual MLPI. The curve is based on the MLPI formulation.



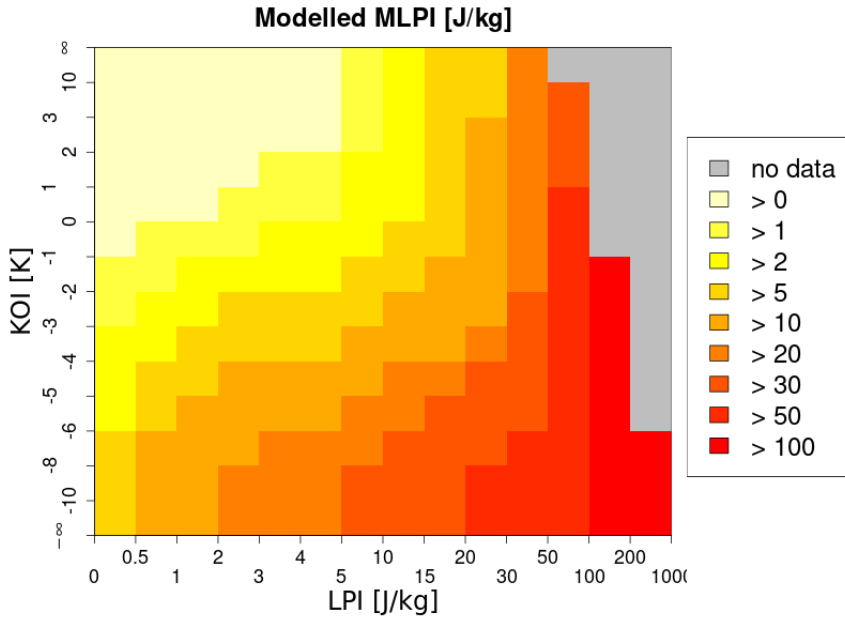


Figure 7: Predicted MLPI per grid cell by LPI and KOI bin using Eq. (1). Bins are the same as in Fig. 3.

Fig. 7 shows the predicted MLPI for the same bins as Fig. 3. Comparing the two figures also reveals that the fit works overall well with an underestimation for small $LPI < 2 \text{ J/kg}$ and $KOI < -4 \text{ K}$.

3. Quality assessment

The quality of LPI and MLPI and other parameterizations for lightning is assessed by computing their resolution. The resolution is part of the decomposed mean squared error (MSE) (Murphy, 1996). Note that the decomposition of the Brier score is a special case of the MSE decomposition applied to probabilities. The resolution measures how well the forecast can discriminate between situations where the observed quantity is low or high. It is computed by grouping the observations together based on bins of the lightning forecast.

Even though we are only dealing with proxies for lightning rate or lightning probabilities, using the resolution as in the decomposition of the MSE is still possible. After all, all proxies could be converted into actual forecasts of lightning rate or probability by applying quantile mapping to convert the corresponding proxy's model climatology to the equivalent observed climatology of the target quantity.

The resolution is computed by sorting the n proxy data points (e.g. LPI) and generating I bins of equal length $n_i = 100,000$ – except for all zeros that go into one bin. Also the bin with the highest proxy data has a length of less 100,000 (i.e. all the remaining data points). The observations (e.g. lightning rate or probability) belonging to the i th bin are averaged to o_i . The

corresponding overall mean of the observations is given by \bar{o} . Then the resolution is computed as

$$\frac{1}{n} \sum_{i=1}^I n_i(o_i - \bar{o})^2.$$

In the following it will be normalized by the variance of the observations $\text{Var}(o)$, to generate human readable numbers.

3.1. Resolution on the grid scale

The resolution is computed for 3 periods – 03/2019-02/2020, 06/2020-07/2020 and 03/2021-08/2021 – as before for member 1 of ICON-EU-EPS. Here, ICON is started from the analysis once per day with a leadtime of up to 24 hours. The hourly data is evaluated using all lead times. Note that the data of 03/2019-02/2020 was used to fit the MLPI. Consequently, for the MLPI only the other two periods provide an out-of-sample verification. Table 1 gives the results for the resolution of LFD, LPI and MLPI. Additionally, the resolution for a standard output variable of the convection scheme – convective rain within one hour – is also provided for 03/2019-02/2020. The resolution is computed for the lightning rate r_{400} as well as for the probability of lightning occurring within one hour in the grid cell. Overall, convective rain is not a good predictor for lightning compared to the other proxies. LPI performs better than LFD. MLPI generally has the highest resolution. This holds for all 3 periods.

Note that the magnitude of the resolution cannot be compared across different time periods, since it depends on the observations. It can only be compared for the different proxies for the same time period.

Figs. 8 and 9 show the binned lightning rates versus the binned proxies. With LPI and MLPI the highest bins reach higher lightning rates than with LFD and convective rain. This further shows the higher forecast quality of LPI and MLPI. The difference between LPI and MLPI is not so obvious in these figures - mainly, because KOI only has an effect for LPI and $\text{MLPI} < 86.16 \text{ J/kg}$. By eye, the difference in this range cannot be spotted.

3.2. Resolution without double penalty problem

For lightning verification on the grid scale a major problem is double penalty. The model might forecast convection at the wrong location or the wrong time. On the grid scale this will be counted as over-forecasting where no lightning was observed, and under-forecasting where lightning was observed. To understand the effect of the location error, the resolution is computed again in a different way. As observations not the original LINET data is used, but the LINET data spatially and temporally rearranged to match the areas where the model forecast is high. For this the temporal uncertainty is ± 2 hours and the spatial uncertainty is a radius of about 100 km.

The rearrangement of the observations works as follows:

1. Sort the observations (lightning rate r_{400}) by magnitude (over all time steps and grid points).

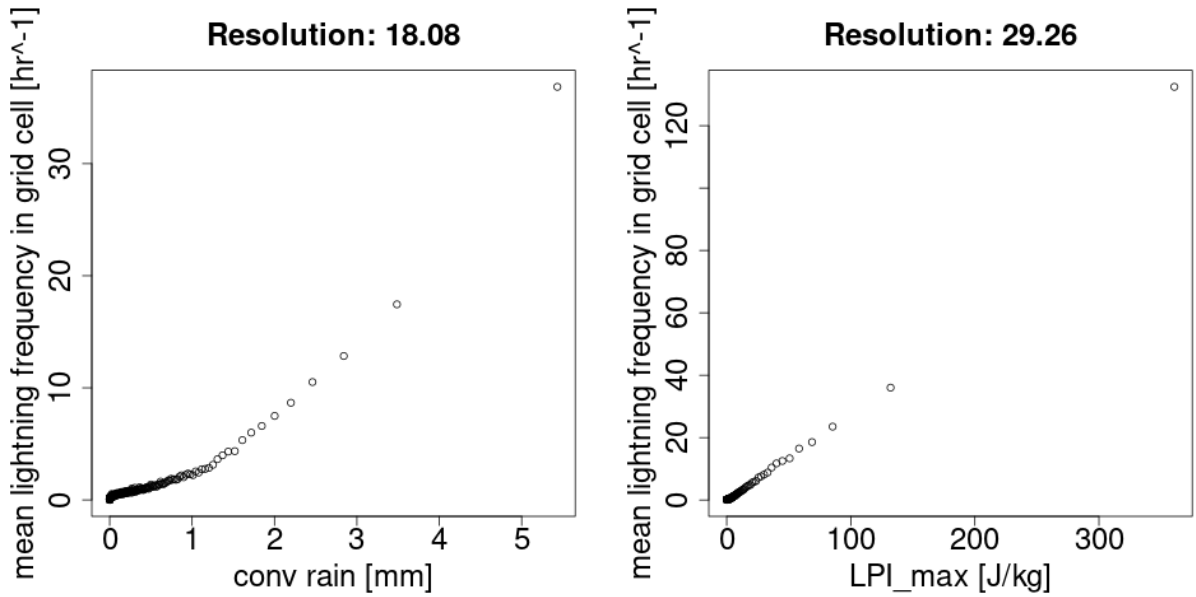


Figure 8: Resolution of convective rain (left) and subgrid scale LPI (right) as proxy for lightning count in grid cell.

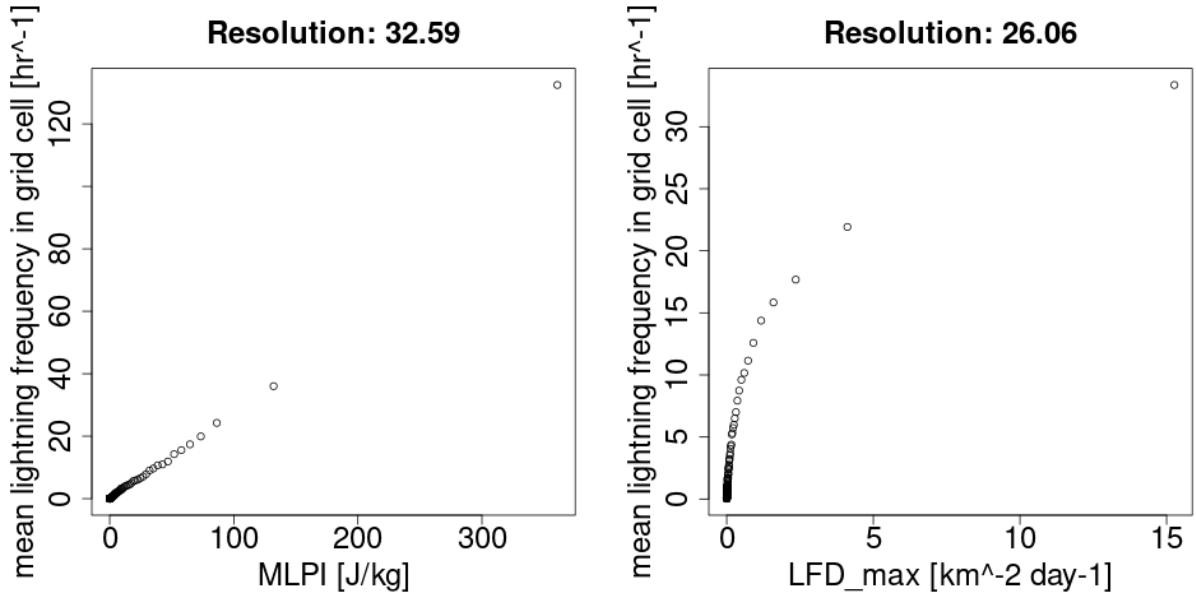


Figure 9: Resolution of modified LPI (left) and LFD (right) as proxy for lightning count in grid cell.

Table 1: Resolution normalized with observation variance for various proxies for lightning.

proxy	resolution	lightning rate	resolution	lightning probability
	03/2019-02/2020		03/2019-02/2020	
convective rain		18.1		6.8
LFD		26.1		9.8
LPI		29.3		10.8
MLPI		32.6		11.6
	06/2020-07/2020		06/2020-07/2020	
LFD		6.9		4.2
LPI		7.1		4.4
MLPI		8.6		5.0
	03/2021-08/2021		03/2021-08/2021	
LFD		15.7		6.6
LPI		15.7		7.0
MLPI		18.0		8.0

2. For a given lightning parameterization all forecasts values (time and space) are marked as "unused".
3. Loop over all data points with $r_{400} > 0$ in descending order.
 - a) Within a radius of 100km and for ± 2 hours look for the time and location of the highest "unused" value in the model forecast.
 - b) The observation is moved to this time and grid point if the forecast is > 0 . If the forecast = 0 the observation remains at its original location.
 - c) The forecast of the new location is marked as "used".

This algorithm is applied to the observations for each lightning parameterization separately. The resulting data set is used to compute the reliability. That means that each parameterization is compared to its own rearranged observational data set. Table 2 lists the results. As expected the resolution goes up for all parameterizations. Moreover, LPI gives the highest scores for this verification. Only for the months 06/07 2020 LFD has a slightly higher score. This shows the effect of KOI in MLPI – areas with low LPI are raised where it is physically plausible – i.e. where KOI is low. This increases the chance to hit areas with observed lightning. Therefore, the main improvement for MLPI compared to LPI is the reduced location error.

4. Climatology

There is insufficient data to estimate the true model climatology and compare it to observations. However, for the given forecast period a comparison can be made. Since the parameterizations do not forecast lightning directly, the forecasts have to be converted to actual lightning. This in

Table 2: Resolution normalized with observation variance for various proxies for lightning.

Here the observations have been temporally and spatially moved to match the model forecast and avoid the double penalty problem.

proxy	resolution lightning rate	resolution lightning probability
	03/2019-02/2020	03/2019-02/2020
LFD	401.8	70.6
LPI	453.7	77.6
MLPI	445.3	71.6
	06/2020-07/2020	06/2020-07/2020
LFD	166.4	40.7
LPI	164.3	40.6
MLPI	163.5	38.5
	03/2021-08/2021	03/2021-08/2021
LFD	355.2	59.3
LPI	362.0	64.6
MLPI	357.0	58.4

itself would require a calibration.

Here the target quantity is a lightning flag – i.e. whether or not lightning is observed in the regular lon/lat grid of 0.2 degrees resolution with the pole rotated to (170°E, 40°N). The observed lightning flag has been computed from LINET data. In the following $L_{i,j,h}$ denotes the lightning flag of the LINET data for grid cell (i, j) during hour h . That means, $L_{i,j,h} = 0$ if no lightning was observed and $L_{i,j,h} = 1$ if lightning was observed.

For the parameterizations the lightning flag can be computed using a threshold. It is not clear which threshold to use, therefore a reasonable approach is to determine a threshold such that over the year and the whole domain the modeled number of cases with lightning flag = 1 is equal to the observed number.

$P_{i,j,h}$ denotes the forecast of the parameterization (i.e. LFD, LPI or MLPI). Since the forecast is uncertain, it makes sense to transform the model forecast not to a 0/1 flag but to some kind of probability $0/p$. This probability p could be a function of the parameterization P . For simplicity in this section it is a constant. Then a simple calibration function C_p is applied with:

$$C_p(P_{i,j,h}) = \begin{cases} 0 & \text{for } P_{i,j,h} < th_p \\ p & \text{for } P_{i,j,h} \geq th_p \end{cases}, \quad (2)$$

with th_p such that

$$\sum_{i,j,h} C(P_{i,j,h}) = \sum_{i,j,k} L_{i,j,h}. \quad (3)$$

Equation (3) ensures that the modeled number of cases with lightning flag = 1 is equal to the observed number. The model data consists of 366 24h hours forecasts from 03/2019 to 02/2020 with ICON-20. Each forecast starts at 00 UTC. Table 3 shows thresholds for 3 probabilities $3^{-1}, 0.5$ and 1 for LFD, LPI and MLPI.

Table 3: Thresholds for the calibration of the lightning parameterizations depending on the probability p in Eq. (2).

p	LFD [day $^{-1}$ km $^{-1}$]	LPI [J/kg]	MLPI [J/kg]
3^{-1}	0.0381	7.14	4.92
0.5	0.0809	11.78	10.99
1	0.2557	23.81	27.72

4.1. Diurnal cycle

For the three thresholds for each lightning parameterization the diurnal cycle is determined computing the number of grid point hours with lightning throughout the year and domain for a given time of day. Note that for the lightning parameterizations for $p < 1$ only the fraction p counts per hour, i.e. for $p = 0.5$ each hour exceeding the threshold th_p counts only half.

Figs. 10 to 12 show the diurnal cycle for $p = 3^{-1}$, 0.5 and 1. All three parameterizations show a too early onset of lightning in the afternoon. In the late afternoon and evening the schemes underestimate lightning compared to LINET. Generally LPI and LFD have the best diurnal cycle while MLPI has a higher maximum and a lower minimum during the day. It can be noticed that there is a local minimum near 1 UTC. This is likely due to the cold start initialization of the model which probably causes some noise leading to convection.

The different values of p have an effect on the diurnal cycle. Lower values of p lead to a less extreme diurnal cycle. This can be explained by the resulting lower thresholds th_p . Times where convection is lower (like morning or evening) have a higher chance to still be counted as lightning. At the same time relatively, the times with larger convection are attributed less lightning. Optimally, as stated before, p should be a function of the values of the lightning parameterization itself.

The shortcomings seen in the diurnal cycle are probably linked to the convection scheme. It is well known that in single column models (SCM) there is the tendency that the diurnal cycle of deep convection is in phase with the surface fluxes (e.g. [Guichard et al., 2004](#)). This issue was mostly removed by [Bechtold et al. \(2014\)](#) through the introduction of a new extended CAPE closure on which the ICON parameterization is based on. However, especially convection in the evening and night is still underestimated (e.g. see Fig. 5 in [Bechtold et al., 2014](#)).

4.2. Annual cycle

Similar to the diurnal cycle Figs. 13 to 15 show the annual cycle based on the period 03/2019 to 02/2020. While LFD and LPI showed similar behavior for the diurnal cycle, they differ in their annual cycle. The maximum in June is more pronounced for LFD and MLPI which are also more similar. Again, increasing p leads to stronger extremes in the annual cycle. For MLPI and LFD $p = 3^{-1}$ gives the best results, while for LPI $p = 0.5$ is optimal.

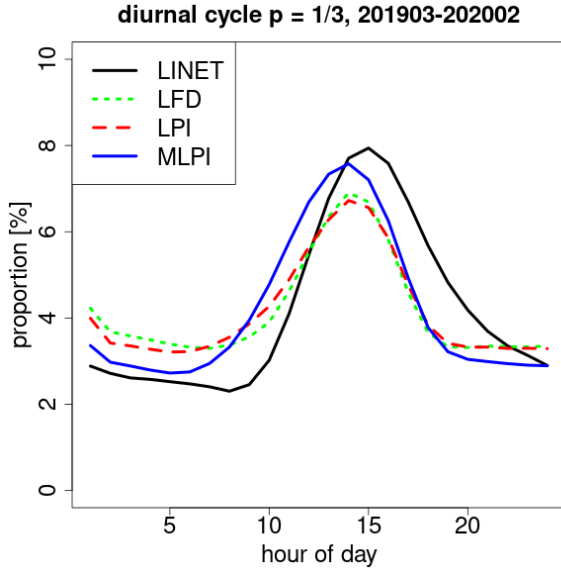


Figure 10: Diurnal cycle for 03/2019 to 02/2020 for LINET (black), LFD (green) LPI (red) and MLPI (blue) for $p = 3^{-1}$. The curves are normalized so that the sum over all hours corresponds to 100 %. Therefore the hourly proportion of the total is shown.

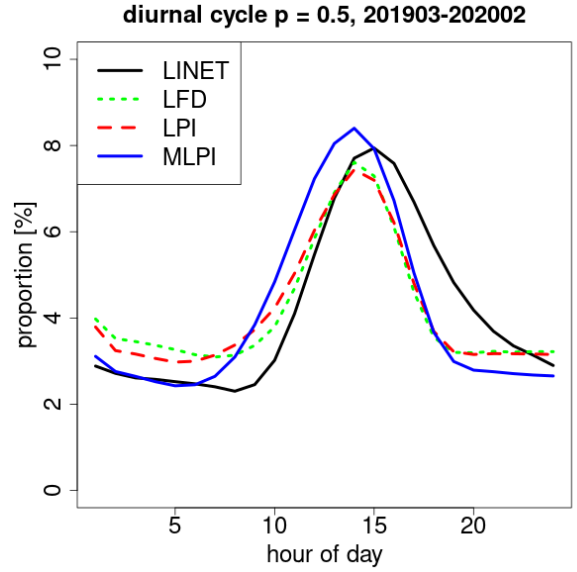


Figure 11: As Fig. 10 but for $p = 0.5$.

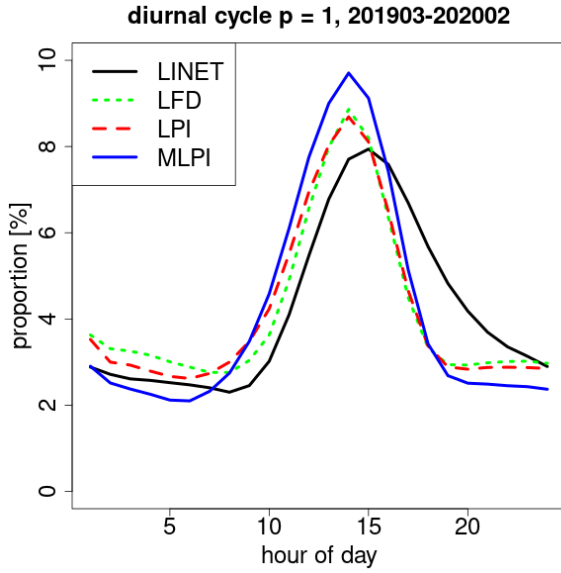


Figure 12: As Fig. 10 but for $p = 1$.

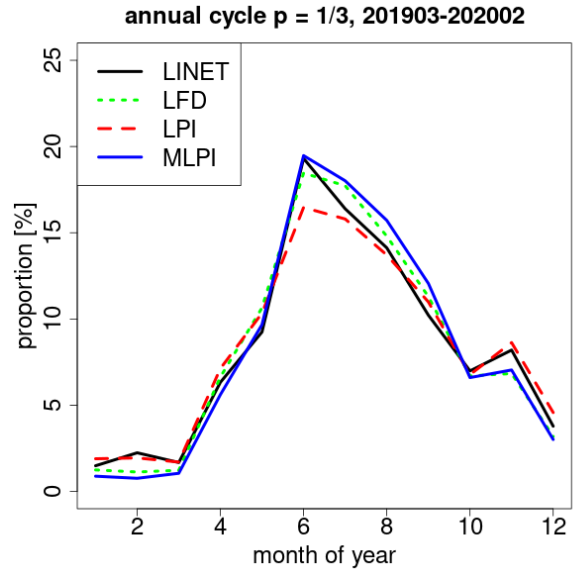
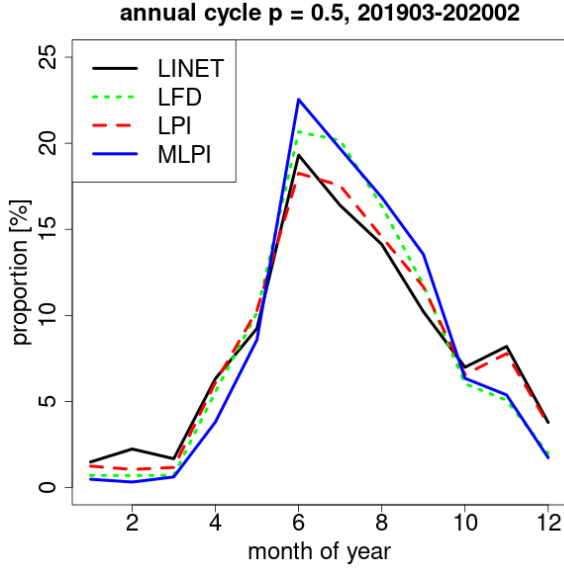
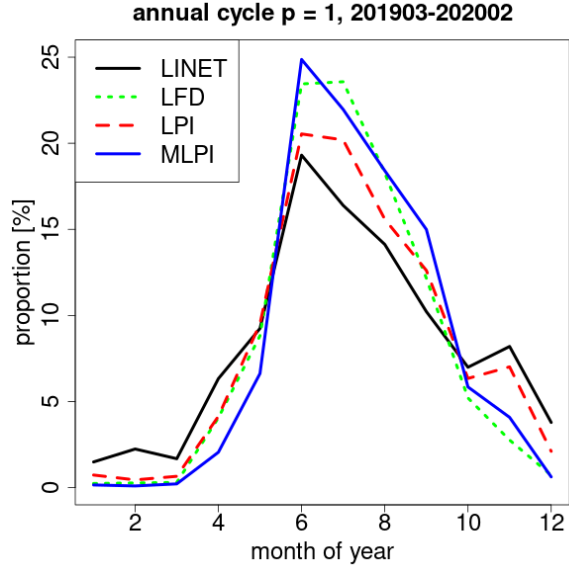


Figure 13: Annual cycle for 03/2019 to 02/2020 for LINET (black), LFD (green) LPI (red) and MLPI (blue) for $p = 3^{-1}$. The curves are normalized so that the sum over all hours corresponds to 100 %. Therefore the monthly proportion of the annual total is shown.

**Figure 14:** As Fig. 13 but for $p = 0.5$.**Figure 15:** As Fig. 13 but for $p = 1$.**Table 4:** Correlation of LINET with parameterizations for one year (03/2019 to 02/2020) for count of grid cell hours with lightning depending on the probability p as in Eq. (2). This corresponds to the data shown in Figs. 16 to 22.

p	LFD	LPI	MLPI
3^{-1}	0.831	0.854	0.883
0.5	0.826	0.867	0.875
1	0.787	0.851	0.852

4.3. Spatial distribution

For the different p the number of hours with lightning for 03/2019 to 02/2020 are counted per grid cell (Fig. 16 to 22). Note that the non-linear scale makes differences in low lightning regions like over the North Sea more visible.

Generally, for all three parameterizations the modeled spatial structure resembles the one observed. However, MLPI has the tendency to be lower in regions with less lightning like over the northern oceans with lower SST such as the North Sea. This could be a negative effect of KOI. The vertical equivalent potential temperature gradient is likely to be less over water with low SST. The optimization for MLPI is such that on average it improves the forecast of all occurred lightning, which will be dominated by the hot spots over land.

By eye the distribution of lightning agrees best with LINET for LFD with $p = 1$, while MLPI and LPI agree better with $p = 3^{-1}$. However, the highest correlation can be found for LFD and MLPI at $p = 3^{-1}$ and for LPI for $p = 0.5$ (Tab. 4). MLPI has generally a higher correlation with LINET than LPI and LFD.

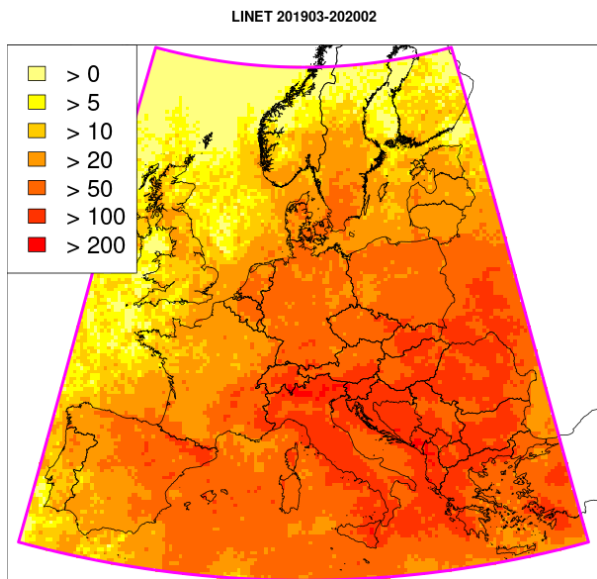


Figure 16: Observed number of hours with lightning per grid cell for 03/2019 to 02/2020 based on LINET data.

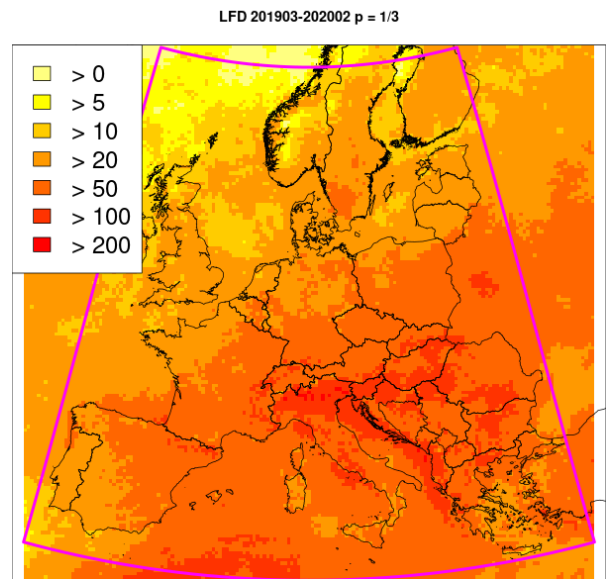


Figure 17: As Fig. 16 but for LFD and $p = 3^{-1}$.

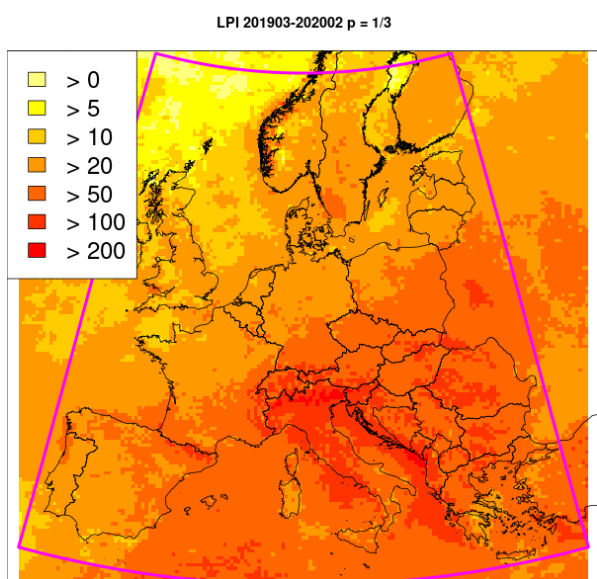


Figure 18: As Fig. 16 but for LPI and $p = 3^{-1}$.

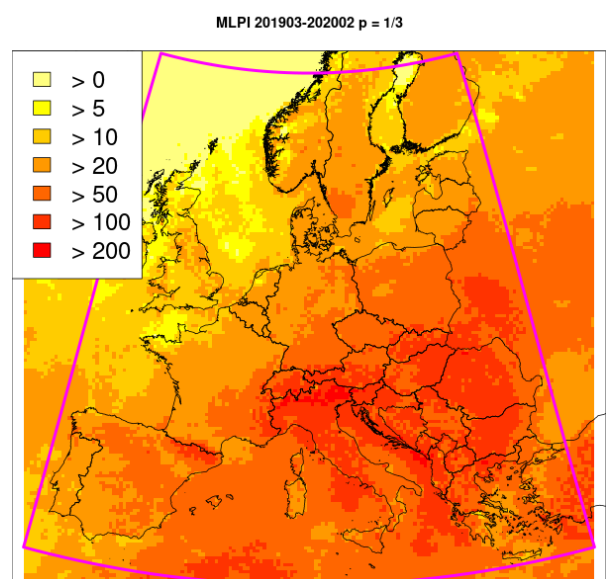
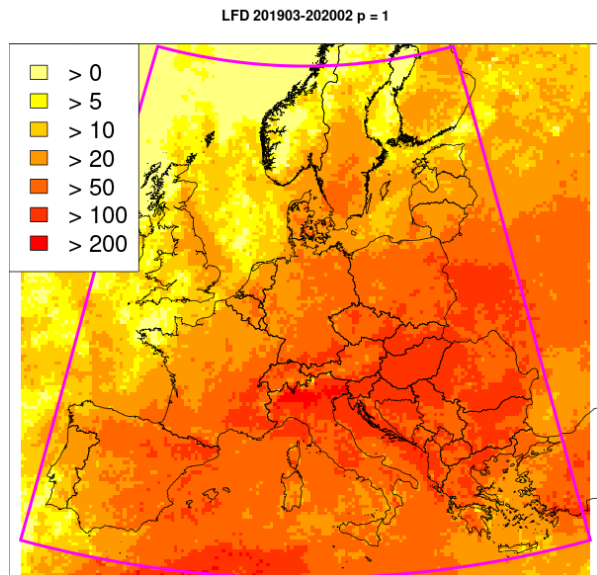
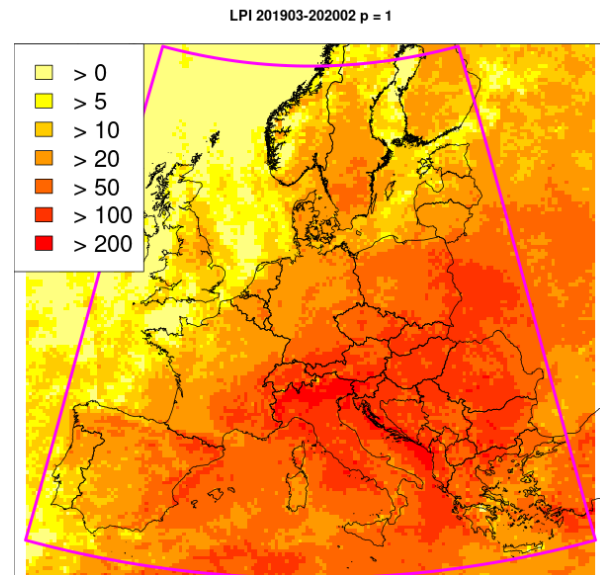
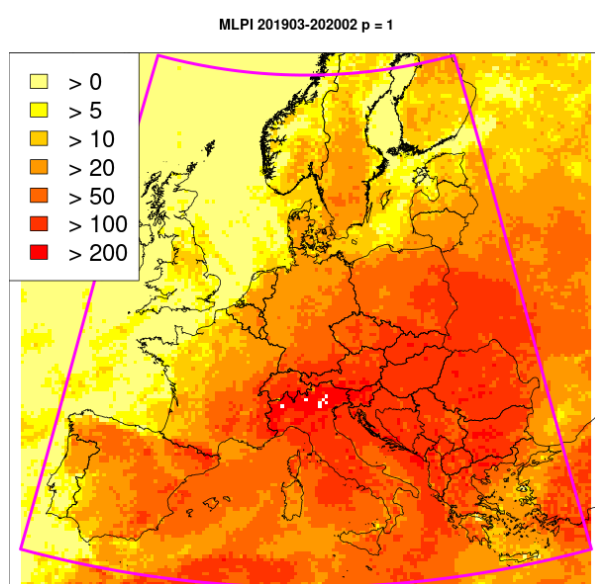


Figure 19: As Fig. 16 but for MLPI and $p = 3^{-1}$.

**Figure 20:** As Fig. 16 but for LFD and $p = 1$.**Figure 21:** As Fig. 16 but for LPI and $p = 1$.**Figure 22:** As Fig. 16 but for MLPI and $p=1$.

5. Case studies

For each season one case study is presented.

5.1. Autumn 18/10/2019

A low pressure system with the center over the British Isles dominates Central Europe. A cold front is passing eastward over central Europe. Ahead of it moist warm air is advected by south westerly winds. Thunderstorms develop along the front. Behind the front moist maritime sub polar air from the Atlantic can be found. Here solar radiation leads to occasional showers with a few embedded isolated thunderstorms. Figs. 23 to 26 show the observed lightning as well as the forecast of an ICON-20 00 UTC run for LFD, LPI and MLPI at 14 UTC. For the LINET observations the lightning count within each $20 \times 20 \text{ km}^2$ grid cell is shown. For the lightning parameterizations the fields are shaded with thresholds as in Tab. 3. All three parameterizations are able to forecast the lightning – though not at the exact location. This is likely due to the front progressing more slowly in the model than in reality. The area of actual lightning is smaller than the shaded areas of the forecasts which is simply due to the way the thresholds have been chosen for the model. By definition, the area exceeding the lowest threshold for a lightning parameterization is 3 times the area observed by LINET – when averaging over one year.

5.2. Winter 10/02/2020

From 09/02/2020 to 10/02/2020 the center of a strong low pressure system (named Sabine in Germany) moved from Scotland to Norway. At 13 UTC its frontal system had already passed over France and Germany. The moist maritime air behind the cold front was prone to showers due to solar heating. Lightning was observed in a band from the English Channel to Poland. The lightning parameterizations simulate this only poorly (Figs. 27 to 30). No lightning is modeled over Germany as the convection scheme is not triggered.

5.3. Spring 13/03/2021

A cold front is passing over central Europe. At 16 UTC it is stretched from southern France to the border of Poland and Germany. Behind it moist maritime polar air is transported from the Atlantic. Solar radiation causes isolated showers with embedded thunderstorms over north west Germany, Benelux and the north east of France. The parameterized lightning covers a smaller area and is mostly concentrated over north east France (Figs. 31 to 34). LPI shows the strongest lightning signal.

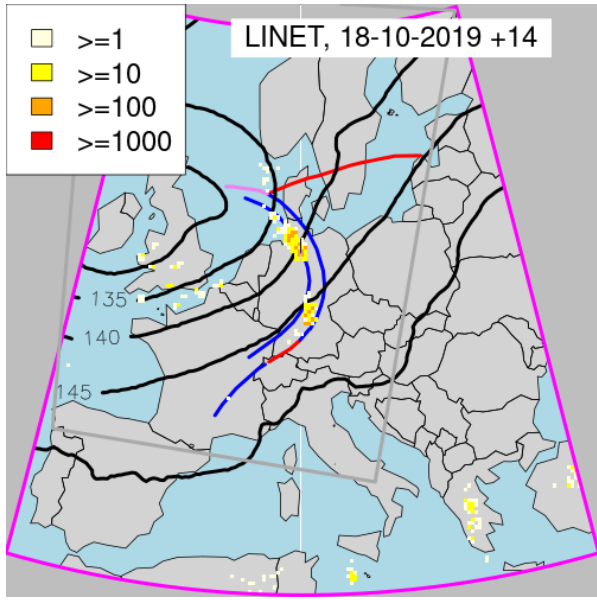


Figure 23: Autumn example: Observed lightning for LINET at 14 UTC 18/10/2019. Shading gives the observed lightning count per $20 \times 20 \text{ km}^2$ grid cell. The LINET domain is outlined by a purple line. The ICON-20 850 hPa geopotential height in 10 m is given by black contour lines (00 UTC run). Within the gray rectangle fronts are marked as warm (red), cold(blue) and occlusion (purple). The fronts were created by DWD forecasters via onscreen analysis (OSA, Vorhersage- und Beratungszentrale - VBZ).

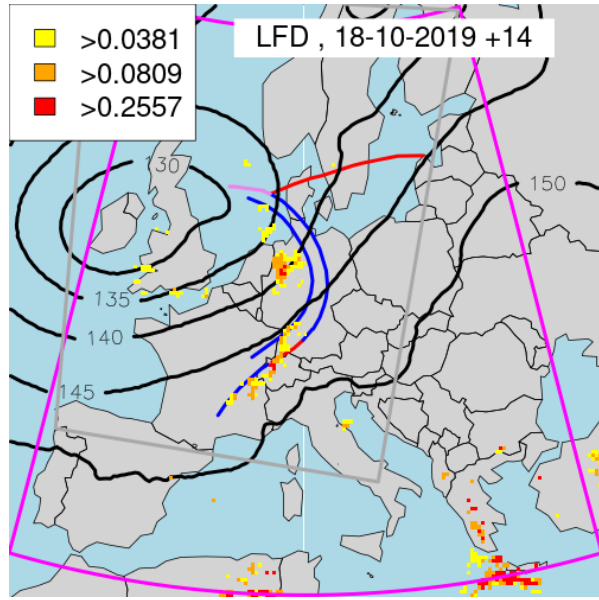


Figure 24: As Fig. 23 only for LFD (00 UTC run). Shading intervals correspond to the thresholds given in Tab. 3.

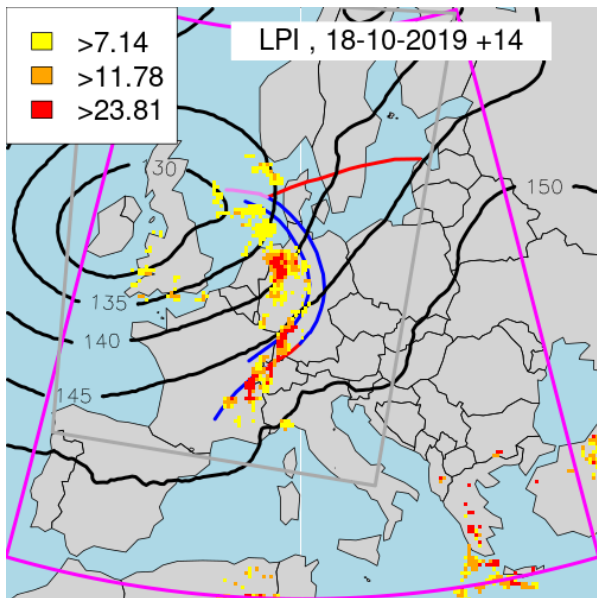


Figure 25: As Fig. 24 but for LPI.

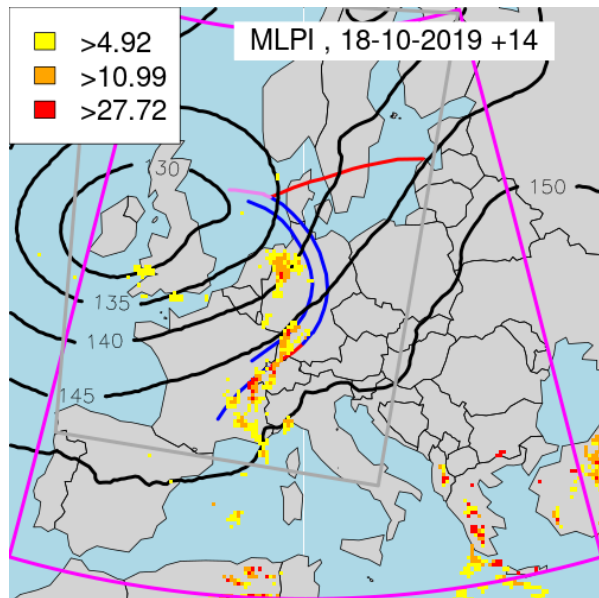


Figure 26: As Fig. 24 but for MLPI.

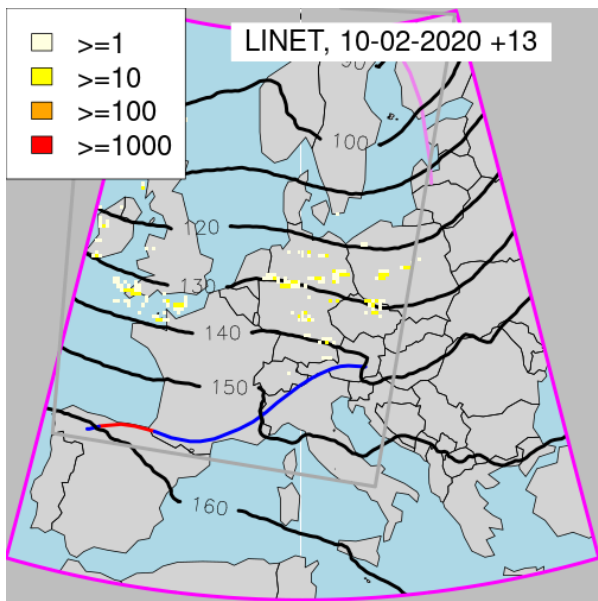


Figure 27: Winter example: As Fig. 23 but for 10/02/2020 13 UTC.

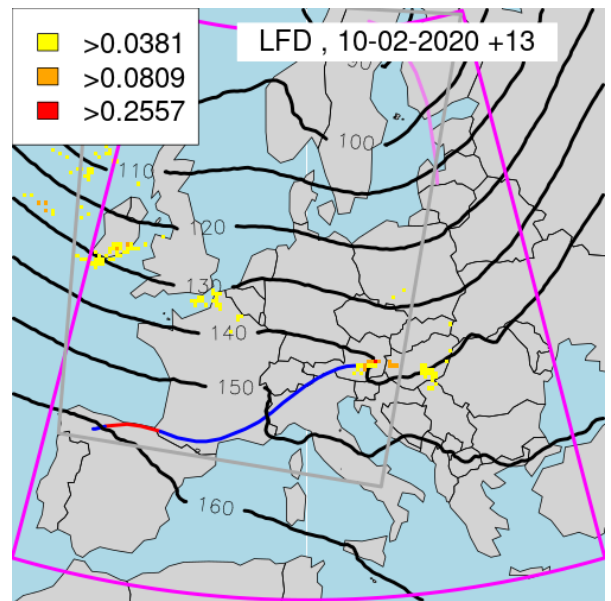


Figure 28: As Fig. 24 but for 10/02/2020 13 UTC.

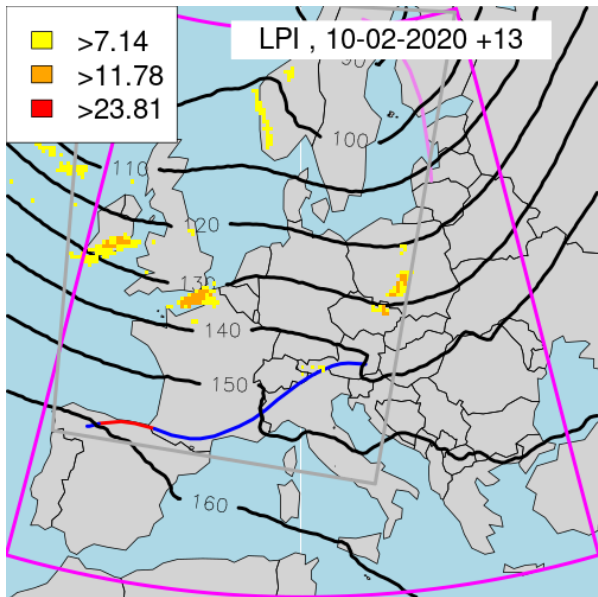


Figure 29: As Fig. 25 but for 10/02/2020 13 UTC.

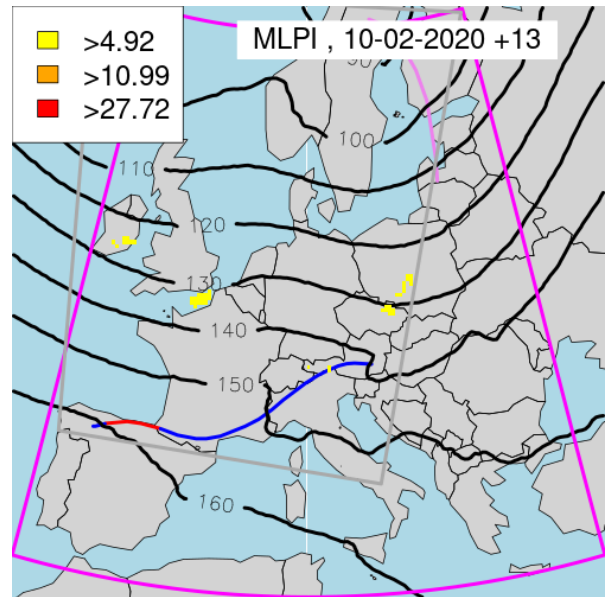


Figure 30: As Fig. 26 but for 10/02/2020 13 UTC.

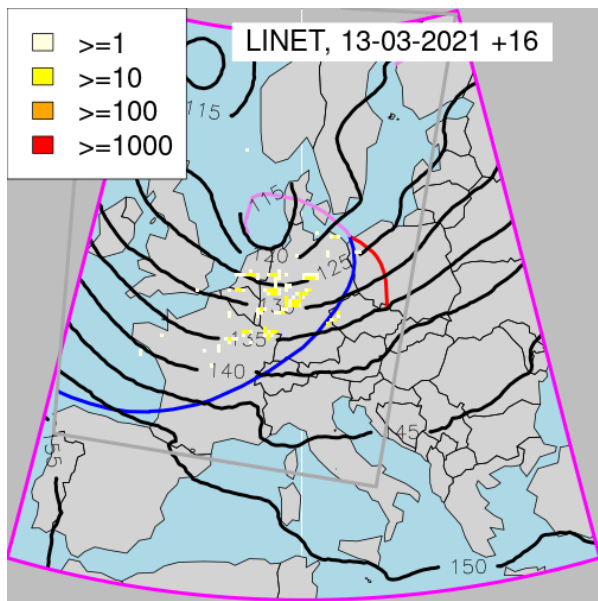


Figure 31: Spring example: As Fig. 23 but for 13/03/2021 16 UTC.

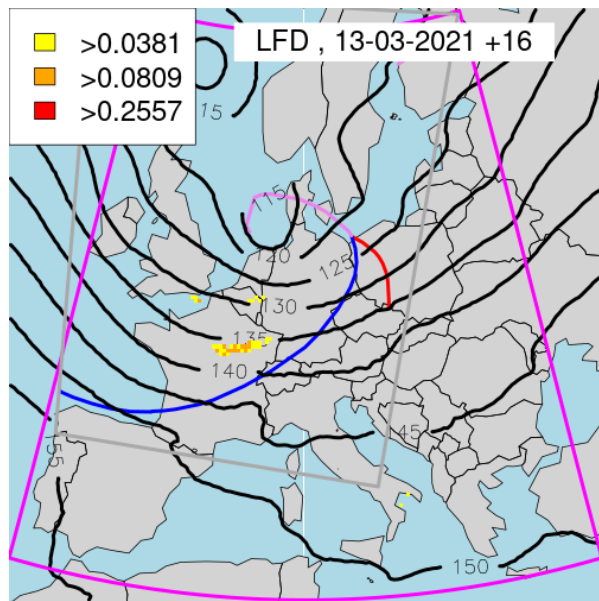


Figure 32: As Fig. 24 but for 13/03/2021 16 UTC.

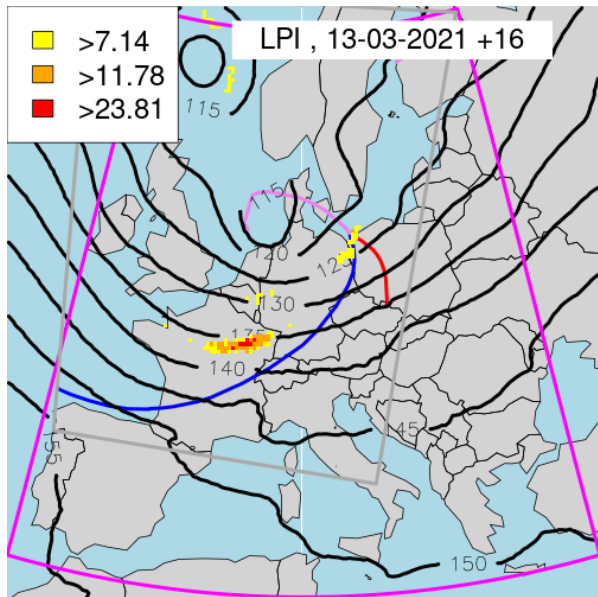


Figure 33: As Fig. 25 but for 13/03/2021 16 UTC.

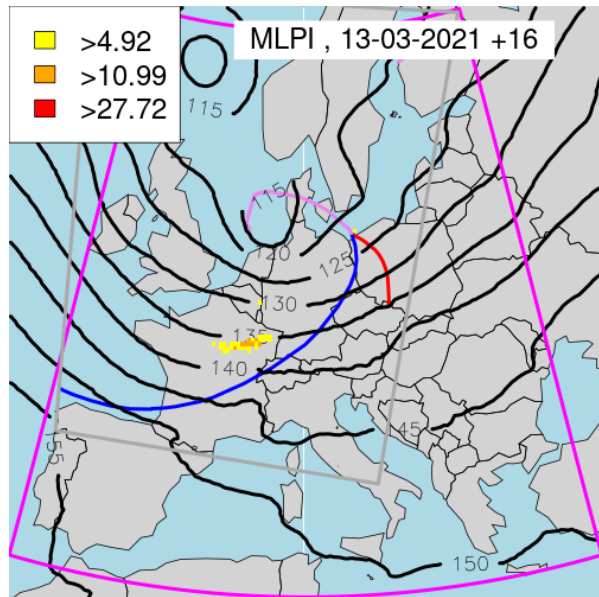


Figure 34: As Fig. 26 but for 13/03/2021 16 UTC.

5.4. Summer 17/07/2021

In the previous days moist subtropical air masses had been transported from the Mediterranean Sea northward by a low pressure system (most prominent at 500 hPa) centered over Germany. During the afternoon thunderstorms develop in an area between southern Italy and Lithuania and Belarus. The area of lightning is depicted well by all parameterization schemes (Figs. 35 to 38). MLPI covers the largest area, LFD covers the smallest area. Note that the shading colors used for LINET (count of lightning) and for the parameterizations (three levels of convection intensity) are not directly comparable in terms of intensity.

6. Summary and Conclusions

Three subgrid scale lightning parameterizations have been implemented in ICON and can be used when run with parameterized deep convection. The lightning flash density (LFD) as in IFS ([Lopez, 2016](#)), the subgrid scale lightning potential index (LPI) adjusted for use with parameterized convection and a modified LPI (MLPI) that uses the KO-Index in conjunction with the LPI. When tested with ICON-20 all three parameterizations are able to simulate lightning that is comparable to what is observed.

For the resolution component of the MSE (or Brier Score for probabilities) the MLPI performs best compared to LFD and LPI. The location error for MLPI is lower since a low KO-index leads to higher MLPI where only weak convection is present in the model. These are often regions where actual convection is still observed.

The onset of the parameterized afternoon convection is on average 1–2 hours earlier than observed. This effect is stronger for MLPI than for LFD and LPI. Depending on the interpretation of the data (i.e. thresholds to define lightning) the annual cycle is best for LPI. MLPI and LFD have the tendency to produce more lightning in the summer months than observed.

The spatial correlation of MLPI with LINET is better than for LFD and LPI in the analysis of lightning occurred during one year. However, over the colder oceans in the north MLPI has a tendency to underestimate the occurrence of lightning.

Case studies show that generally the parameterizations have a tendency to underestimate lightning occurring behind cold fronts when moist maritime air is present. Lightning in warm moist air masses as observed in summer months is simulated well.

Given the findings above the LFD, LPI and MLPI are useful tools to assess where lightning could occur in the numerical model forecast. When the model result is interpreted on grid scale, MLPI is the recommended parameterization. However, when the location error is not important LPI is more recommendable as it has a higher resolution. In general all three indices could help forecasters with a quick evaluation of the synoptic situation and could be used for automated forecast products. Another field of application could be climate simulations to assess if trends in lightning can be attributed to climate change. The indices could also potentially facilitate the assimilation of lightning observations into ICON (Köpken-Watts 2021, personal communication).

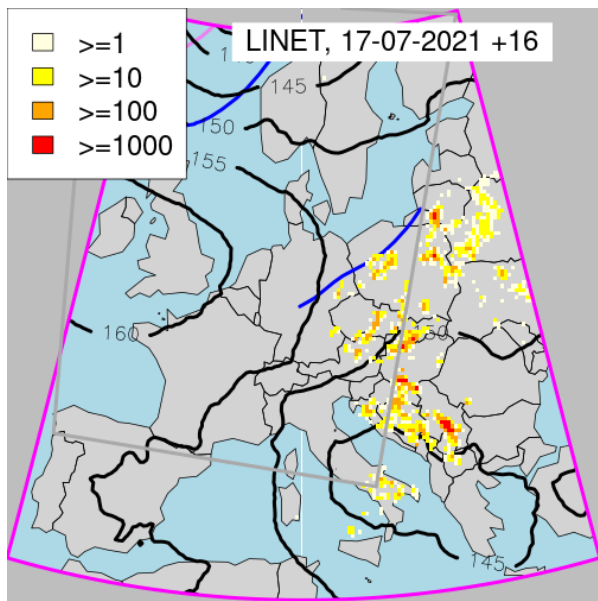


Figure 35: Summer example: As Fig. 23 but for 17/07/2021 16 UTC.

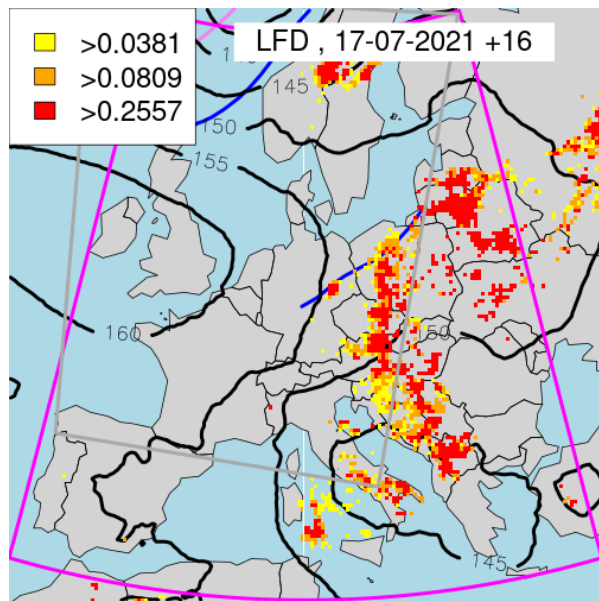


Figure 36: As Fig. 24 but for 17/07/2021 16 UTC.

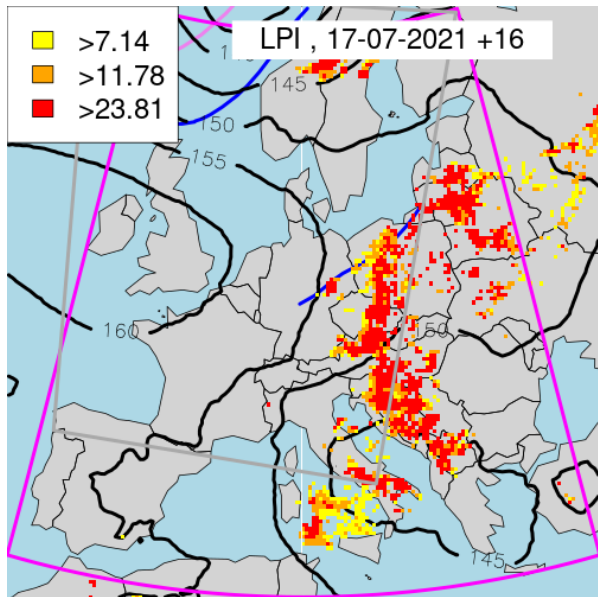


Figure 37: As Fig. 25 but for 17/07/2021 16 UTC.

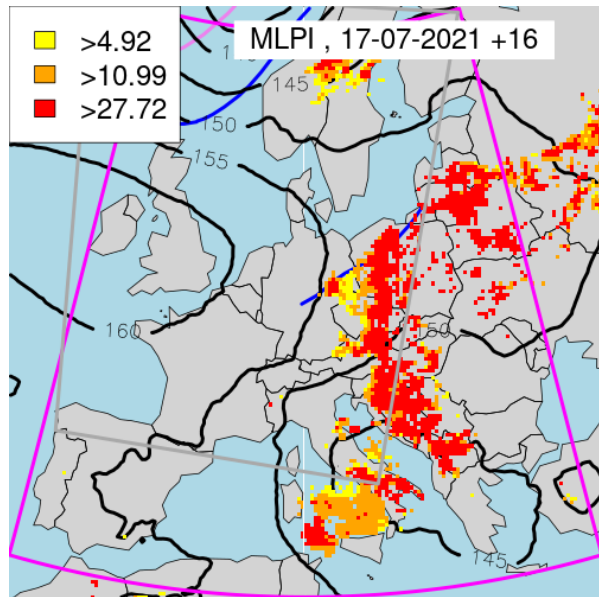


Figure 38: As Fig. 26 but for 17/07/2021 16 UTC.

The findings in this report furthermore show the potential for further calibration with post-processing. Since temporal and spatial uncertainty is inevitable when forecasting lightning for larger lead times, this could be addressed by applying optimal temporal and spatial upscaling.

7. Acknowledgments

The authors would like to thank the European Severe Storms Laboratory (ESSL, <https://www.essl.org>) for the evaluation of the MLPI and fruitful discussions. Thanks also go to Daniel Reinert for supporting the implementation into ICON, to Linda Schlemmer for supporting the operationalization and for reviewing this report and to Sebastian Borchert and Sibylle Krebber for requesting WMO GRIB codes for the subgrid scale LPI. Thanks go to Berliner Wetterkarte (<https://www.berliner-wetterkarte.de>) whose charts greatly helped to analyze past synoptic situations. All data analysis and plots were done with the R script language (R Core Team, 2019).

References

- Bechtold, P., 2017: *Atmospheric moist convection*. ECMWF, Reading, UK, 85 pp., URL https://www.ecmwf.int/sites/default/files/elibrary/2017/Atmospheric_moist_convection.pdf.
- Bechtold, P., M. Köhler, T. Jung, F. Doblas-Reyes, M. Leutbecher, M. Rodwell, F. Vitart, and G. Balsamo, 2008: Advances in simulating atmospheric variability with the ECMWF model: From synoptic to decadal time-scales. *Q. J. R. Meteorol. Soc.*, **134**, 1337–1351, URL <https://doi.org/10.1002/qj.289>.
- Bechtold, P., N. Semane, P. Lopez, J.-P. Chaboureau, A. Beljaars, and N. Bormann, 2014: Representing equilibrium and nonequilibrium convection in large-scale models. *J. Atmos. Sci.*, **71**, 734–753, URL <https://doi.org/10.1175/JAS-D-13-0163.1>.
- Betz, H., K. Schmidt, P. Laroche, P. Blanchet, W. P. Oettinger, E. Defer, Z. Dziewit, and J. Konarski, 2009: LINET - an international lightning detection network in europe. *Atmos. Res.*, **91**, 564–573, URL <https://doi.org/10.1016/j.atmosres.2008.06.012>.
- Charn, A. B., and H. Parishani, 2021: Predictive proxies of present and future lightning in a superparameterized model. *Journal of Geophysical Research: Atmospheres*, **126** (17), 1–16, URL <https://doi.org/10.1029/2021JD035461>.
- Guichard, F., and Coauthors, 2004: Modelling the diurnal cycle of deep precipitating convection over land with cloud-resolving models and single-column models. *Q. J. R. Meteorol. Soc.*, **130** (604), 3139–3172, URL <https://doi.org/10.1256/qj.03.145>.
- Lopez, P., 2016: A lightning parameterization for the ECMWF Integrated Forecasting System. *Mon. Weather Rev.*, **144**, 3057–3075, URL <https://doi.org/10.1175/MWR-D-16-0026.1>.
- Lynn, B., and Y. Yair, 2010: Prediction of lightning flash density with the WRF model. *Adv. Geosci.*, **23**, 11–16, URL <https://doi.org/10.5194/adgeo-23-11-2010>.
- McCaul, E. W., S. J. Goodman, K. M. LaCasse, and D. J. Cecil, 2009: Forecasting lightning threat using cloud-resolving model simulations. *Weather and Forecasting*, **24** (3), 709 – 729, URL <https://doi.org/10.1175/2008WAF2222152.1>.
- Murphy, A. H., 1996: General decomposition of MSE-based skill scores: Measures of some basic aspects of forecast quality. *Mon. Weather Rev.*, **124**, 2353–2369, URL [https://doi.org/10.1175/1520-0493\(1996\)124<2353:GDOMBS>2.0.CO;2](https://doi.org/10.1175/1520-0493(1996)124<2353:GDOMBS>2.0.CO;2).
- R Core Team, 2019: *R: A Language and Environment for Statistical Computing*. Vienna, Austria, R Foundation for Statistical Computing, URL <https://www.R-project.org/>.
- Stoltz, D. C., S. A. Rutledge, J. R. Pierce, and S. C. van den Heever, 2017: A global lightning parameterization based on statistical relationships among environmental factors, aerosols, and convective clouds in the TRMM climatology. *J. Geophys. Res.: Atmos.*, **122**, 7461–7492, URL <http://dx.doi.org/10.1002/2016JD026220>.
- Taszarek, M., J. T. Allen, H. E. Brooks, N. Pilguy, and B. Czernecki, 2021: Differing trends in United States and European severe thunderstorm environments in a warming climate. *Bulletin of the American Meteorological Society*, **102** (2), E296 – E322, URL <https://doi.org/10.1175/BAMS-D-20-0004.1>.

Tippett, M. K., and W. J. Koshak, 2018: A baseline for the predictability of U.S. cloud-to-ground lightning. *Geophysical Research Letters*, **45** (19), 10 719–10 728, URL <https://doi.org/10.1029/2018GL079750>.

Ulbrich, S., 2016: Estimation of convective extreme events over Germany based on large scale parameters. Dissertation, Universität Köln, 129 pp., URL <http://kups.ub.uni-koeln.de/id/eprint/7065>.